IEEE Access
Multidisciplinary | Rapid Review | Open Access Journal

Received July 23, 2020, accepted August 18, 2020, date of publication September 3, 2020, date of current version September 21, 2020.

Digital Object Identifier 10.1109/ACCESS.2020.3021458

Investigation of Mn Doped ZnO Nanoparticles Towards Ascertaining Myocardial Infarction Through an Electrochemical Detection of Myoglobin

MAZHARUL HAQUE[1], HASSAN FOUAD[2,3], HYUNG-KEE SEO[4], ALOTHMAN Y. OTHMAN[5], ATUL KULKARNI[6], AND Z. A. ANSARI[1]

[1]Centre for Interdisciplinary Research in Basic Science, Jamia Millia Islamia, New Delhi 110025, India
[2]Applied Medical Science Department, Community College, King Saud University, Riyadh 11433, Saudi Arabia
[3]Biomedical Engineering Department, Faculty of Engineering, Helwan University, Helwan 11792, Egypt
[4]School of Chemical Engineering, Jeonbuk National University, Jeonju 54896, South Korea
[5]Chemical Engineering Department, College of Engineering, King Saud University, Riyadh 11433, Saudi Arabia
[6]Symbiosis Centre for Nanoscience and Nanotechnology, Symbiosis International University, Pune 412115, India

Corresponding author: Z. A. Ansari (zaansari@jmi.ac.in)

This work was supported by the Deanship of Scientific Research at King Saud University, Saudi Arab, through the Research Group under Grant RG–1435-52. The work of Mazharul Haque was supported by the Indian Council of Medical Research (ICMR), New Delhi, through the Senior Research Fellowship, under Grant 45/54/2018-NAN/BMS.

ABSTRACT Mn-doped ZnO nanostructures were synthesized with three different estimated Mn concentration (atoms/cm^3) using sol-gel technique. As synthesized nanostructures were analyzed using X-ray diffraction spectroscopy (XRD), Fourier-transform-infrared spectroscopy (FTIR), and field-emission secondary electron microscopy (FE-SEM). XRD pattern reveals of doped ZnO nanostructures reveal a peak related to $Zn_2Mn_3O_8$ phase along with peaks related to pure ZnO. Average particle size, estimated using Scherer formula, increases with Mn-doping. FE-SEM reveals morphological change from spherical particles ($\sim$15-20 nm) to nano-rods then nano-belt like 2 D super lattice structure after doping. Optical band gap obtain from Tauc's plot is 3.82, 2.05, 2.1 and 2.47 eV for pure-ZnO and Mn-doped samples with 13×10^{17}, 20×10^{17} and 32×10^{17} Mn atoms/cm^3, respectively. Presence of vibration band from 665 to 680 cm^{-1} in FTIR spectra endorses metal oxide formation. Nanomaterials were screen printed over working electrode of pre-fabricated three terminal electrode. This was used for electrochemical detection of myoglobin (Mb); a biomarker for acute myocardial infarction and were tested for Mb concentrations from 0-15 nM using cyclic voltammetry and electrochemical impedance spectroscopy. Redox current and charge transfer resistance varied linearly with Mb concentration. 7-fold increased sensitivity towards Mb in Mn-doped ZnO sensors is attributed to doping induced stress in nanostructures. Maximum sensitivity of 95μA-cm^{-2} nM^{-1} with LOD of 0.35 nM is observed for ZnO with 13 $\times$ 10^{17} Mn atomic/cm^3. Response time of $\sim$10 ms is observed. Interference carried out with 7 nM Cytochrome c and 5 mM HSA reveal different oxidation potential and current value for Mb.

INDEX TERMS Acute myocardial infarction, biomarker, electrochemical, metal oxides nanoparticles, myoglobin sensor.

I. INTRODUCTION

ZnO nanostructures have emerged as prominent material in the field of semiconductors and is intensively investigated for variety of device applications. Doping of transition metal ions in ZnO is evident to modulate the physical properties which are useful for varied applications including gas sensing, optical, opto-electronic, piezoelectric and photocatalytic device applications and for DNA sequence detectors owing to induced defect states [1]–[6]. Transition metal doped ZnO is investigated to detect acute myocardial infarction (AMI) in early stage of onset symptoms owing to potential physical and electronic properties.

AMI, commonly known as heart attack is remained an utmost cause of death globally [7]–[10]. AMI is irreversible necrosis causes cardiovascular diseases (CVD) that

The associate editor coordinating the review of this manuscript and approving it for publication was Lei Wang.

include stroke, heart failure (HF), rhythm disorders, congenital heart disease, valvular disease, subclinical atherosclerosis, coronary heart disease (CHD), venous disease, peripheral artery disease and secondary irreversible coronary ischemia. The number of deaths caused by CVD is highest and defeat that of overall death caused by chronic respiratory diseases and all forms of cancers. According to WHO over 17.9 million people lose their lives every year due to CVD from 2016 to 2018 that estimates 31% of total deaths globally, 75% of which occurs in low-middle income countries owing to high economic cost of cure [11, 12]. The statistical update of American Heart Association 2019 estimated that yearly about 350,000 people in the US suffer from cardiac arrest outside the hospital with a 90% mortality [12]. European Cardiovascular Disease Statistics 2017 revealed that annually 3.9 million death in Europe occurred with total 1.8 million in European Union (EU) itself scaled to total 45% death in Europe and 37% in EU caused by CVD [13]. Besides various initiatives for the awareness and fight against CVD by WHO and World heart Federation, the statistical projections predict approximately 23.6 million deaths amid to CVDs by 2030 [11]–[13]. According to a report, during 2016 about 62.5 million in India and 12.7 million in United States lost their life at an early age owed to CVD. The estimated age-standardized prevalence of CVD in India was 5,681 per 100,000. However, owing to India's population, the absolute estimated prevalence of CVD of 54.6 million is over 60% higher than 33.6 million in United States [14]. Early stage diagnosis of CVD is crucial for identification and successful prediction of the CVD diseases which assures appropriate treatment for patient CVD treatment and survival and saving cost and time [11]–[14].

Established method of CVD diagnosis include initial focused physical examination-evaluation, electrocardiogram (ECG) followed by a brief history, radiography, and testing biomarkers in the blood, are time consuming. ECG is faster and play a crucial role for the treatment, but has inconsistency in diagnosis as most of the patients in emergency unit exhibit normal ECG limits [15]. Detection of biomarkers at the start of CVD is vital not only for early prompt diagnosis but also for patient survival and successful prognosis of the diseases with cost effectiveness. Some of the biomarkers that are detected in CVD patients with stroke are brain natriuretic peptide, fibrinogen, C-reactive protein, lipoproteins and their components [8] and neutrophil gelatinase-associated lipocalin [9], [10]. Additionally, proteins that are released in the blood stream with the inception of CVD progression and are potential cardiac biomarkers are myoglobin (Mb), troponin I, creatine kinases (CK-MB) and Copeptin [16]–[18]. Mb (∼18kD), which generally found in blood stream following muscle injury is widely suggested as one of the relevant markers for an early diagnosis of AMI [19]–[21]. Mb is released within an hour of AMI symptom and attain maximum level in 2 h [22]–[28]. On the other hand, troponin I and CK-MB release only after 4 h and 6 h, respectively, whereas Copeptin is difficult to quantify owing to its very short half-life [29]. Mb level consequently increases from 70 ng/ml (4 nM) to 200 ng/ml (11 nM) within 90 min [11], [18] unlike troponin I and CK-MB which remain normal. Therefore, Mb detection can be a key measure in clinical diagnosis of cardiac injury in an early period of CVD inception. Physiological range of Mb is (70-200 ng ml^{-1}) narrow and require highly sensitive system to detect below 70 ng/ml and beyond 200 ng/ml [30]. Mb is composed of 154 amino-acid residues, 8 α-helices and a heme protein which carries the oxygen to muscle tissues. Redox-pair of Fe-ion in heme protein can be utilized for potent electrochemical detection of Mb.

Techniques such as immunoassays [31], SPR sensor [32], [33], optical-fiber biosensor [34], colorimetric determination using PDMS-AuNPs film [35], chemoluminescence based ELISA [26], electrochemical immunosensors [22], [27], [36] and other electrochemical methods [37]–[41] are utilized for Mb detection. Although, these are selective owing to specific receptors/recognition element but require bulky laboratory setup with trained manpower, expensive, time consuming and tedious [42]. Development of rapid, portable and highly sensitive technological platform for CVD diagnosis with easily operable clinical parameter is need of the time which can be economically viable to poor economical people [11], [12].

Amongst the available advanced sensing techniques, electrochemical sensors provide versatile platform for biosensors and are used for detection, diagnosis and managements of diseases like diabetes with low cost, simple to operate with high degree of selectivity, reversibility and high sensitivity.

Recently, range of engineered nanostructured materials including metal, semiconductor and insulator are fabricated to improve the charge transfer characteristics and selective interaction of biomolecules for the feasible label-free detection through electrochemical biosensors. Nanomaterials emerged as promising potential candidate for electrochemical matrix due to inherent high surface area to volume ratio, excellent electrical conductivity, fast electron transport characteristics, high thermal conductivity and enhanced sensitivity [43]. Nanomaterials and their composites are tailored as unique platform for detection of cardiac markers. Wei Sun *et al.* reported NiO and graphene modified carbon electrode for electrochemical detection of Mb between 0.69 to 30.0 mM [44]. X. Ren *et al.* investigated gold nanoparticle based immunosensor to detect Mb from 350 ng-ml^{-1} to 17.5 μg-ml^{-1} exhibited lowest limit of detection (LOD) of 5.5 ng-ml^{-1} [45]. Sun *et al.* studied an electrochemical impedance response of Ag-Mb in phosphate buffer solution (pbs) where Mb ranges from 10 ng-ml^{-1} to 1 μg-ml^{-1} with LOD of 2.7 ng-ml^{-1} [46]. Zhang *et al.* used CuS–MoS_2 functionalized Anti-MYO for Mb detection between 0.005 to 20 ng-ml^{-1} reported LOD of 1.2 pg-ml^{-1} [47]. Mandal *et al.* studied TiO_2 nanotube modified glassy carbon electrode (GCE) to detect Mb between 0.001- 0.1 mg-ml^{-1} with LOD of 1 μg-ml^{-1} [48]. Kumar *et al.* used rGO/CNT modified SPE electrode for Mb detection which exhibit

linear response from 1 ng-ml^{-1} to 4 mg-ml^{-1} with LOD of 0.34 ng-ml^{-1} [49]. Wang *et al.* used ionic-liquid electrode modified by Fe_3O_4 coated on SiO_2 microsphere for electrochemical Mb detection between 0.2 to 11.0 ng-ml^{-1} with LOD of 0.18 ng-ml^{-1} [50].

In this work, Mn-doped ZnO nanoparticles synthesized with three different Mn-doping concentrations (atomic fractions) were characterised for structural and morphological examinations using XRD, FTIR, and FESEM. A feasibility study was done using these nanoparticles to detect nanomolar (3–15 nM) Mb biomarker for acute myocardial infraction at early onset of the symptoms using screen printed electrodes (SPEs) via electrochemical technique i.e. cyclic-voltammetry (CV) and electrochemical impedance spectroscopy (EIS).

II. EXPERIMENTAL DETAILS

A. MATERIAL SYNTHESIS AND CHARACTERIZATION

Zinc acetate dehydrate ($(CH_3COO)_2.Zn._2H_2O$, 98%), manganese acetate tetra hydrate ($(CH_3COO)_2Mn.4H_2O$, 99%) and NaOH were acquired from Loba Chemicals Pvt. Ltd., India. Myoglobin (100684-32-0), Cytochrome c (9007-43-6) and HSA (70024-90-7) were procured from Sigma Aldrich, USA. For phosphate buffer $NaH_2PO_4.2H_2O$, 98% and Na_2HPO_4, 99% (Fischer Scientific, India). Deionized Millipore water (DI, 18 MΩ resistivity) was used to prepare all the solutions. Mn doped ZnO was synthesized following method reported earlier [51].

Atomic fraction of Mn doping concentration was pre-estimated based on the ratio of Mn atoms to that of native Zn atoms. Stock solution of 1mM Mn precursor was separately prepared in ethanol and used. The atomic fractions are estimated as 13×10^{17} (S1), 20×10^{17} (S2), and 32×10^{17} (S3) of Mn atoms/cm^3 for doping in ZnO matrix. The required Mn concentration was obtained by systematic addition of manganese acetate solution to make up 0.31, 0.45, and 0.73 mM, respectively, in three different reactions whereas pristine ZnO (S0) was synthesized without adding Mn solution.

In a typical reaction, 17 mg of zinc acetate was dissolved in 200 ml DI water (2.25 mM) as a main precursor in which an estimated volume of manganese acetate from 1mM stock (in ethanol) was mixed under continuous stirring, to acquire final concentration of 0.31, 0.45 and 0.73 mM making of total 200 ml solution to attain atomic fractions of 13×10^{17}(S1), 20×10^{17} (S2) and 32×10^{17} (S3) Mn atoms/cm^3 in ZnO matrix, respectively. To this, 35 ml of 2.33 mM NaOH (ethanol solution) was added dropwise in 30 min during constant stirring. Mixture was refluxed at 80 °C for 3 h to get uniform growth and cooled naturally. Obtained crystals were washed several times with DI water followed by drying in air convection oven at 70 °C for 12 h. For pristine ZnO nanoparticles (S0), the process was repeated without adding manganese acetate solution. Fine powder was obtained in a mortar-pestle to be used further.

Structural analysis of as synthesized nanostructured powders was performed using Cu-Kα ($\lambda = 1.542$ Å) as an X-ray radiation source in the X-ray diffractometer (Ultima IV, Rigaku). Diffraction pattern was acquired for the Bragg's angle from 20° to 80° at 40 keV source voltage and 30 mA current. Average particle size 'D' were estimated using Scherer's formula:

$$D = 0.9\lambda/\beta_{hkl}cos\theta \tag{1}$$

λ is the wavelength of X-ray source CuK_α, β is full width at half of the maxima at Bragg angle θ.

The induced crystals strain during the growth, owed to 5% lattice mismatch between Mn and Zn, was estimated from Williamson-Hall (W-H) relation [52]. FTIR spectra of as synthesized powders and their solution with 15 nM Mb, were obtained in ATR mode (Tensor 37, Bruker), to investigate the change in surface functional group with Mb. Surface morphology was scrutinized by field emission scanning electron microscopy (FESEM, SU 70, Hitachi). UV-Vis absorption spectra was obtained between of 225-450 nm for all nanostructured particles before and after addition of 15 nM Mb using U3900 spectrophotometer (Hitachi) from optimized concentration of 100 μg synthesized nanoparticle in 2 ml phosphate buffer.

B. FABRICATION OF ELECTROCHEMICAL SENSOR

A pre-fabricated three terminal (working, counter and reference) gold plated Cu electrode (SPE) were used to prepare electrochemical sensor. Working electrode (dia. 4 mm, area 0.13 mm^2) was coated with screen printed film of synthesized nanostructures using conventional screen printing [53],[54]. Thixotropic paste was prepared using nanomaterial powder by mixing organic binders viz. ethyl cellulose (EC) and butyl carbitol acetate (BCA) in 70:30 ratio [55]. Printed electrodes were kept to settle for 10 minutes and dried in oven at 60 °C for 4 h.

10 ml stock solution of 100 mM Mb was prepared in PBS (phosphate buffer, pH = 7.2) and further serially diluted to obtained a range of concentrations from 3 nM to 15 nM (3, 5, 7, 10, 12 and 15 nM) and used to test. The range was selected to cover complete physiological range of Mb in the blood from 70 ng-ml^{-1} (4 nM) to 200 ng-ml^{-1} (12 nM). Lower limit side detection i.e. below 70 ng-ml^{-1} is significantly important to monitor deficiency in O_2 supply to the skeletal cardiac muscles.

C. ELECTROCHEMICAL SENSOR CHARACTERIZATION

Cyclic voltammogram of all electrodes were acquired with PBS as reference followed by different Mb concentrations viz. 3 nM, 5 nM, 7 nM, 10 nM, 12 nM and 15 nM. Voltammograms were obtained by sweeping the voltage from −1.0 V to +1.0 V at a fixed scan rate (100 mV/s) using V63121 potentiostat (IVIUM Tech., The Netherlands). The oxidation peak current density was plotted with Mb concentration used as a calibration curve that can help to determine the unknown

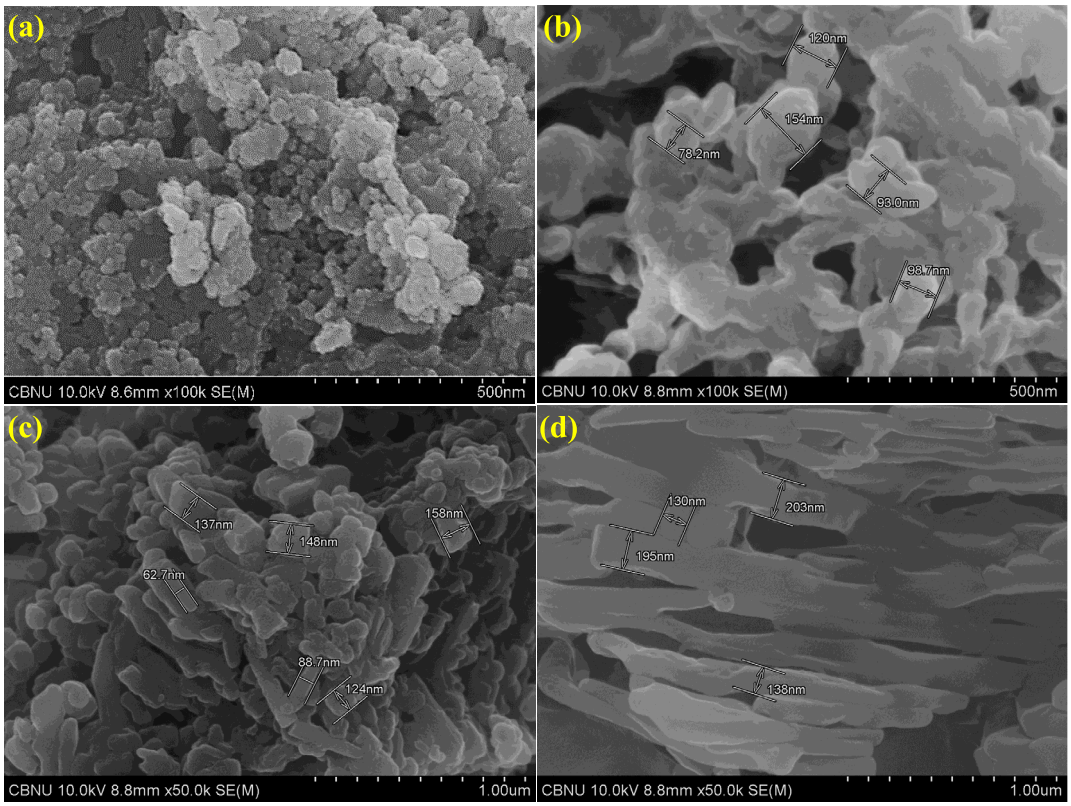

FIGURE 1. Field emission scanning electron microscope (FESEM) micrographs depicting the shape and size of the as synthesized nanomaterial (a) pristine ZnO (S0) (b) ZnO-Mn (S1, 13 × 10^{17}) (c) ZnO-Mn (S2, 20 × 10^{17}) (d) ZnO-Mn (S3, 32 × 10^{17}).

concentration of Mb. Further, charge transfer kinetics of pristine and doped ZnO was investigated using different scan rates ranging from 10 to 100 mV/s at a fix concentration (7 nM). The measurement was repeated for all SPE fabricated using pristine and Mn-doped ZnO. The peak current of the samples was plotted with square root of scan rate to ascertain the charge transfer features. An electrochemical impedance spectroscopy (EIS) was performed using potentiostat in the frequency range of 0.5Hz–10^6 Hz at 50 mV amplitude for all fabricated sensor.

Interference study was conducted on S1 sample with HSA and cytochrome c being small heme-protein and former is abundant in blood plasma. CV curves were obtained in PBS, cytochrome c (7 nM), 7nM Mb and 5 mM HSA in PBS as reference. The data was also recorded for solution by mixing 1:1 volumetric ratio of cytochrome c and Mb as well as Mb and HSA solution, separately, to ascertain the interference.

All the measurements of CV and EIS were carried out at room temperature with an optimized volume of 30 μl of an analyte (Mb/cytochrome c/HSA) solution of each concentration was used separately.

III. RESULTS AND DISCUSSION

A. MATERIAL ANALYSIS

Fig.1 (a-d) depicts FESEM micrograph of as synthesized pristine ZnO (S0) and Mn-doped ZnO (S1-S3) acquired at an accelerating voltage of 10 keV exhibit uniform-sized nano-material evenly distributed over the area. Fig. 1(a) reveal spherical particles of 10-20 nm for pristine ZnO along with some agglomerated particles of ∼30-35 nm. Mn-doping initially transform spherical to oval shaped nanoparticles of ∼70 nm for S1 (Fg.1(b)) which for S2 are agglomerated and grown to rod like structure with diameter of ∼60-150 nm and (Fig. 1(c)) whereas it transmuted to nanobelt like 2D super-lattice structure with highest Mn-doping concentration in S3 as evident from Fig.1(d). This lead by tensile strain as incoming molecules doesn't remain flat and tend to diffuse towards the rough surfaces which are the growth front resulting in the fast growth along a direction forming nanobelts. The increased dimension of nanoparticles at high density of Mn in ZnO matrix in comparison to that of pristine ZnO is due to the induced tensile strain resulting from 14% and 9.5% mismatch in atomic and crystal radii, respectively, between dopant Mn and Zn in the system.

Fig. 2(a) depicts the XRD patterns for pristine and Mn-doped ZnO. Pristine ZnO XRD (S0; lack curve) reveal diffracted peaks with minimum peak intensity related to (110), (100), (202), (002), (311) planes of ZnO as per standard JSPDS file nos. 21-1486, 89-0510, 89-1397, 89-0311. XRD pattern of Mn-doped ZnO nanostructures exhibit diffracted peaks corresponding to (101), (012), (103), (202), (105) and (312) plane of ZnO. Besides peak related to (111) and (015) ZnO phases, a complex Mn-Zn oxide i.e. $Zn_2Mn_3O_8$ is identified using JCPDS card 32-1472.

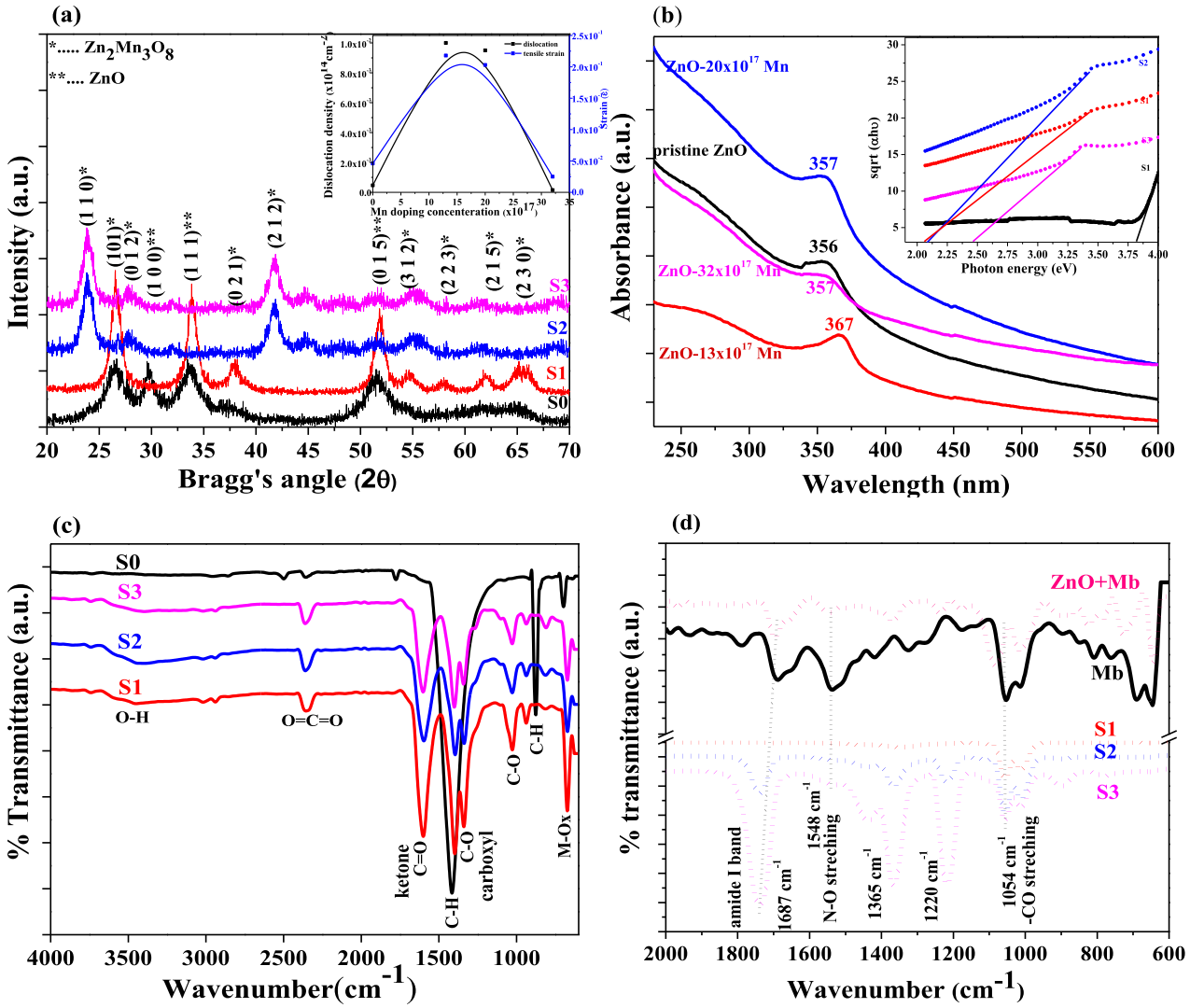

FIGURE 2. (a) X-ray diffraction pattern (XRD) of pristine and Mn doped ZnO nanoparticles (b) UV-Vis absorption spectra and the Tauc's plot in the inset (c) FTIR spectra of undoped and Mn doped ZnO nanoparticles (d) FTIR spectrum of synthesized nanoparticles with Mb; [S0 = pristine ZnO, S1= 13 × 10^{17} Mn atoms/cm^3; S2 = 20 × 10^{17} Mn atoms/cm^3; S3 = 32 × 10^{17} Mn atoms/cm^3].

The peaks related to (111) and (015) plane of ZnO shifted within 2% of Δd values for S1 (red curve) and new peaks related to composite oxide $Zn_2Mn_3O_8$ planes (021), (312), (223), (215) and (230) appeared. In S2 and S3 (212), distinct peaks with maximum intensity to composite (110) and (212) phase of $Zn_2Mn_3O_8$ implies growth in these directions whereas intensity of diffraction peak related to (015) is drastically reduce against S1. The crystallinity of synthesized powders in different directions is reflected from intensity of diffraction peaks. Average particle size (D) of as synthesized nanoparticles estimated using Debye-Scherer's formula (equation (1)) that varies from 70-90 nm where S3 samples exhibit largest size (Table 1). The estimated particles size is in agreement to that obtained from FESEM micrographs. The tensile strain (ε) in the nanocrystals as estimated using Williamson-Hall (W-H) relation, $\varepsilon = \beta_{hkl}/4\tan\theta$ provides maximum value for S1 samples and reduces further with increase of Mn atomic fractions in ZnO matrix as evident from graph of strain versus doping concentration in inset of Fig. 2(a) (black curve). This implies Mn doping initially result in strained crystals later the strain gets compensated at high density of Mn atoms in the system and alters the orientation of crystal growth as evident from XRD. The dislocation density (γ), estimated from $\gamma = 1/D^2$, increases initially then fall out with increasing Mn following the same trend as that of tensile strain as seen from blue curve in inset Fig. 2(a). This reflects, Mn doping at lower concentration knock out or dislocate Zn ions in the matrix results in high dislocation density and relaxing strain at high Mn concentration lead fall of dislocation density.

The optical band gap of the synthesized nanostructures was estimated from UV-Vis spectra acquired in the wavelength range of 225 to 450 nm, Fig. 2(b). The peak absorption for S0 (black curve), S2 (blue curve) and S3 (purple curve) is

TABLE 1. Estimated parameters for sensors.

ZnO with Mn doping concentration (atoms/cm^3)	Optical band gap (eV)	Grain size* (nm)	Dislocation density (x10^{14}cm^{-2})	Strain ε	Sensitivity (μAcm^{-2} nM^{-1})	Limit of Detection (nM)
0	3.59	35	28	0.035	13	2.88
13x10^{17}	1.95	70	46	0.046	95	0.35
20x10^{17}	2.03	78	49	0.218	94	0.39
32x10^{17}	2.10	90	42	0.203	92	0.42

*estimated from Debye-Scherer's formula

almost constant centered at 356-357 nm whereas the peaks is red shifted by 10 nm for S1 (red curve). A red shift of 10 nm suggests the incorporation of deep levels originated from the induced tensile strain effectively leads the reduction of the band gap. Besides, nanoparticles agglomeration may result some additional contribution as is evident from FESEM images (Fig. 1(b)). The direct band gap value estimated from the Tauc's plot i.e. $(\alpha h\nu)^{1/2}$ versus $(h\nu)$, shown as inset of Fig. 2(b), demonstrate reduction in bandgap from 3.82 eV for S0 to lowest value of 2.05 eV as obtained for S1 amongst all synthesized nanostructure owing to the stress induced deep level states and are correlated to induce tensile strain and density of states.

Fig. 2(c) depicts the FTIR spectra of as synthesized doped and un-doped ZnO nanostructures. A broad band recorded around 665-680 cm^{-1} belongs to the finger print region of metal oxides, proves the successful synthesis of ZnO. A peaks around 867 cm^{-1} is correlated to C-H bending whereas a peak at 1410 cm^{-1} belongs to C-O stretching. A peak at 2350 cm^{-1} assigned to CO_2 stretching which is adsorbed from the atmosphere. A broad band spread from 3400-3500 cm^{-1} is correlated to O-H stretching and is significantly increased in Mn doped nanostructures suggesting the remittance of some hydroxide in the system. A low energy C-H peak (867 cm^{-1}) is disappeared and a new C-O peak evolved at $\sim$1054 cm^{-1} whereas a huge peak at 1410 cm^{-1} observed in S0 replaced by a peak related to carboxyl (C-O) and a ketone (C=O) each in Mn doped ZnO samples S1-S3 indicate the change in the surface functional groups lead by doping. Maximum peak intensity observed in S1 reduces further in S2 and S3 lead by reduced density of states.

A feasibility study of synthesized nanostructured materials were carried out for electrochemical detection of low concentration Mb and analysis was done by FTIR studies to characterize variation of the surface functional group (Fig. 2(d)) and optical properties are studied by UV-Vis absorption (Fig.3(a-d)) for pristine and Mn doped ZnO.

FTIR spectra of 15 Mb concentration in PBS (pH 7.4) was recorded (black curve) as a reference whereas FTIR spectra of un-doped and Mn-doped ZnO obtained by adding 15 nM Mb to monitor the alteration in surface functional properties of nanostructures as well as protein conformation, [40], [41]. Spectra of Mb (black curve) reveals a peak at 1054 cm^{-1} related to C-O stretching with a broad peak at 1548 cm^{-1} due to N-O stretching associated to amide I band, C=O stretching at 1687 cm^{-1} and a peak at frequency lower than 800 cm^{-1} is attributed to heme presence in Mb. The red curve is that of pristine ZnO with 15 nM Mb which exhibit the peaks at 1696 cm^{-1}, 1548 cm^{-1} and 1054 cm^{-1} corresponds to amide I band, N-O and C-O stretching, respectively (Fig. 2(d)). However, the functional characteristics of Mn-doped ZnO in presence of 15 nM Mb is changed wherein additional peaks at 1220 cm^{-1} and 1365 cm^{-1} related to C-O and OH-stretching, respectively, are observed. This can be associated to the presence of comparatively high hydroxyl group as also evident from the spectra of doped nanoparticles in Fig.2(c). A slight blue shift of the peaks related N-O and amide I group with increase of intensity of these two and others peaks are observed as a function of increasing Mn concentration in the ZnO matrix. The shift in the peaks (Fig.2(d)) is correlated to either the decrease of bond length in the presence of Mn in the system during interaction with Mb or due to the carboxyl group on nanoparticle surface owing to density of states on the surface which is highly sensitive to environment/vicinity [42].

Fig.3(a-d) present four different sets of systematic absorption study for each nanoparticles with different amount of Mb solution to achieve the concentration of 3-15 nM were carried in PBS (pH 7.4) at a fixed amount of ZnO nanoparticles (20 μg/2 ml). Black curve in all case depicts the spectra of pure or Mn-doped ZnO free of Mb. In presence of Mb, absorption spectra reveal a peak related to ZnO at 265 nm along with a peak at 409 nm that indicate characteristic absorption of myoglobin originates from Soret-band of heme prosthetic group in the center [56]. The systematic decrease in peak absorption intensity of ZnO and gradual increase of that of Mb peak (409 nm) were clearly observed in all four set of graphs with increased Mb concentration

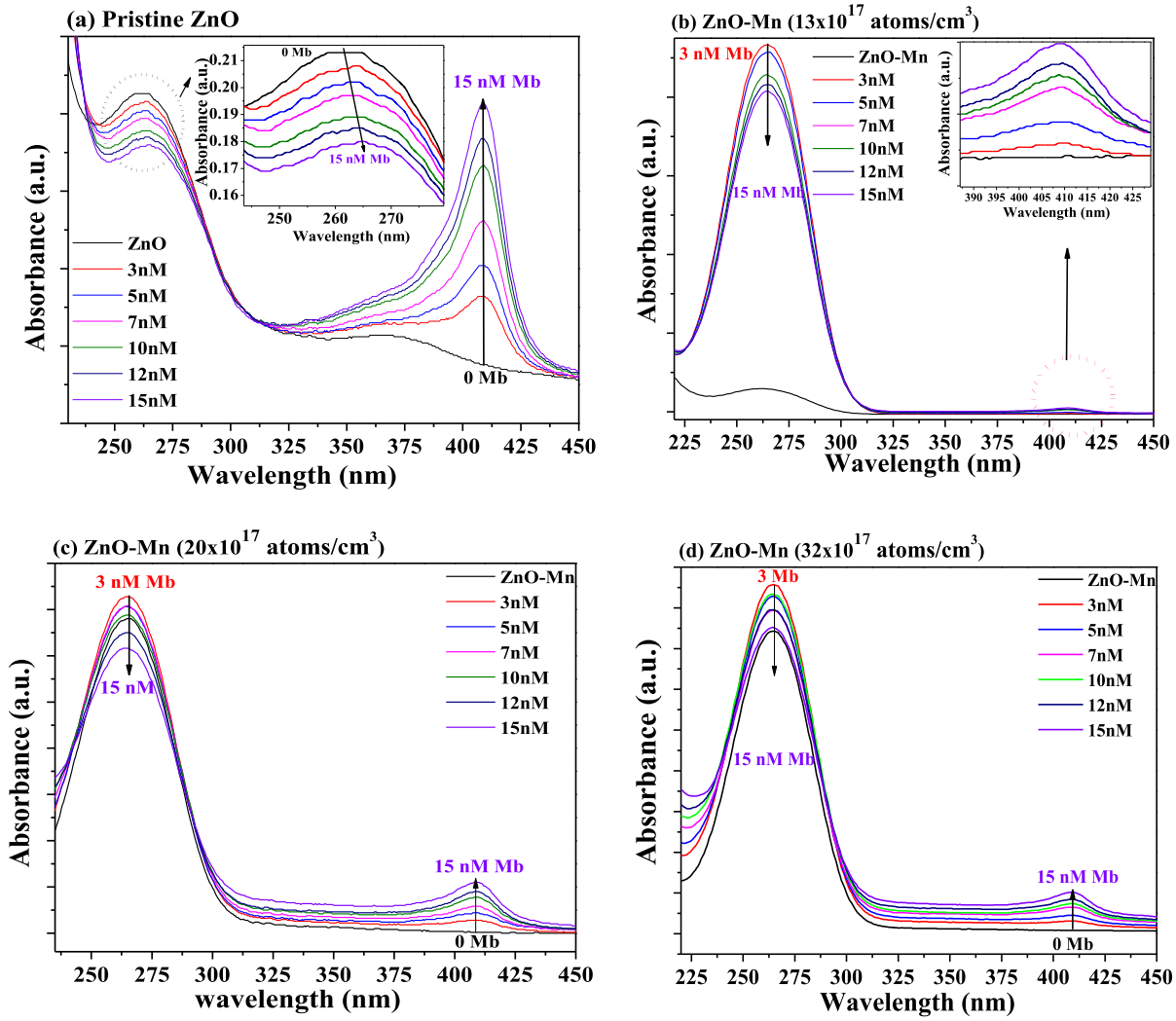

FIGURE 3. Series of UV-vis absorption spectra of synthesized ZnO nanopowders with various Mb concentrations for (a) S0; pristine ZnO (b) S1; ZnO with Mn (13 × 10^{17}) (c) S2; ZnO with Mn (20 × 10^{17}) and (d) S3; ZnO with Mn (32 × 10^{17}).

(Fig. 3(a)-(d)). The increase in absorption value at 409 nm is attributed to the contribution from the free/unbounded Mb molecules present in the solution. In addition, for pure ZnO hypochromic shift of ∼ 4-5 nm is observed with Mb concentration as highlighted in the inset of Fig. 3(a) unlike Mn doped ZnO. Decrease of peak absorption intensity of pure and doped ZnO indicates the formation of nanoparticles-protein conjugate as apparent from FTIR spectra (Fig. 2(d)). Such variation of Soret band is reported earlier by Mandal *et al.* [38].

B. SENSOR CHARACTERIZATION

The electrochemical characteristics of the fabricated SPE were examined by sweeping the applied potential between −1V to +1V at an scan rate of 100 mV/s for different Mb concentrations using a potentiostat. Fig.4 (a-d) represents the voltammogram of pristine (S0) and doped ZnO (S1-S3) for Mb concentration ranging from 3-15 nM in phosphate buffer. In general, pristine and Mn doped ZnO appears to be practically reversible having the gradual increase in peak oxidation and decrease in reduction current. The dotted curve depicts the response of electrode in the phosphate buffer and was treated as reference. Fig. 4(a) reveal the oxidation peaks associated with blue shift towards high applied voltage from 0.025 V to 0.05 V whereas the reduction peak voltage remains constant with increasing Mb concentration from 3 nM to 15 nM. For Mn doped ZnO, the oxidation peak broadens with slight shift towards high applied voltage whereas reduction peak potential remains almost constant as seen from Fig.4(b)-(d). The oxidation peak potential increased from 0.12 V to 0.18V and a small hump appeared around 0.36 V which is clearly seen beyond 7 nM Mb concentration. On the other hand, reduction peak potential changed from −0.28 V to −0.62 V with increasing Mb concentration. Similar trend is followed for Mn doped ZnO samples (S1-S3). Increase in width of oxidation peak implies the change in the electron transfer characteristics with Mb concentration. The current values and width of both oxidation and reduction

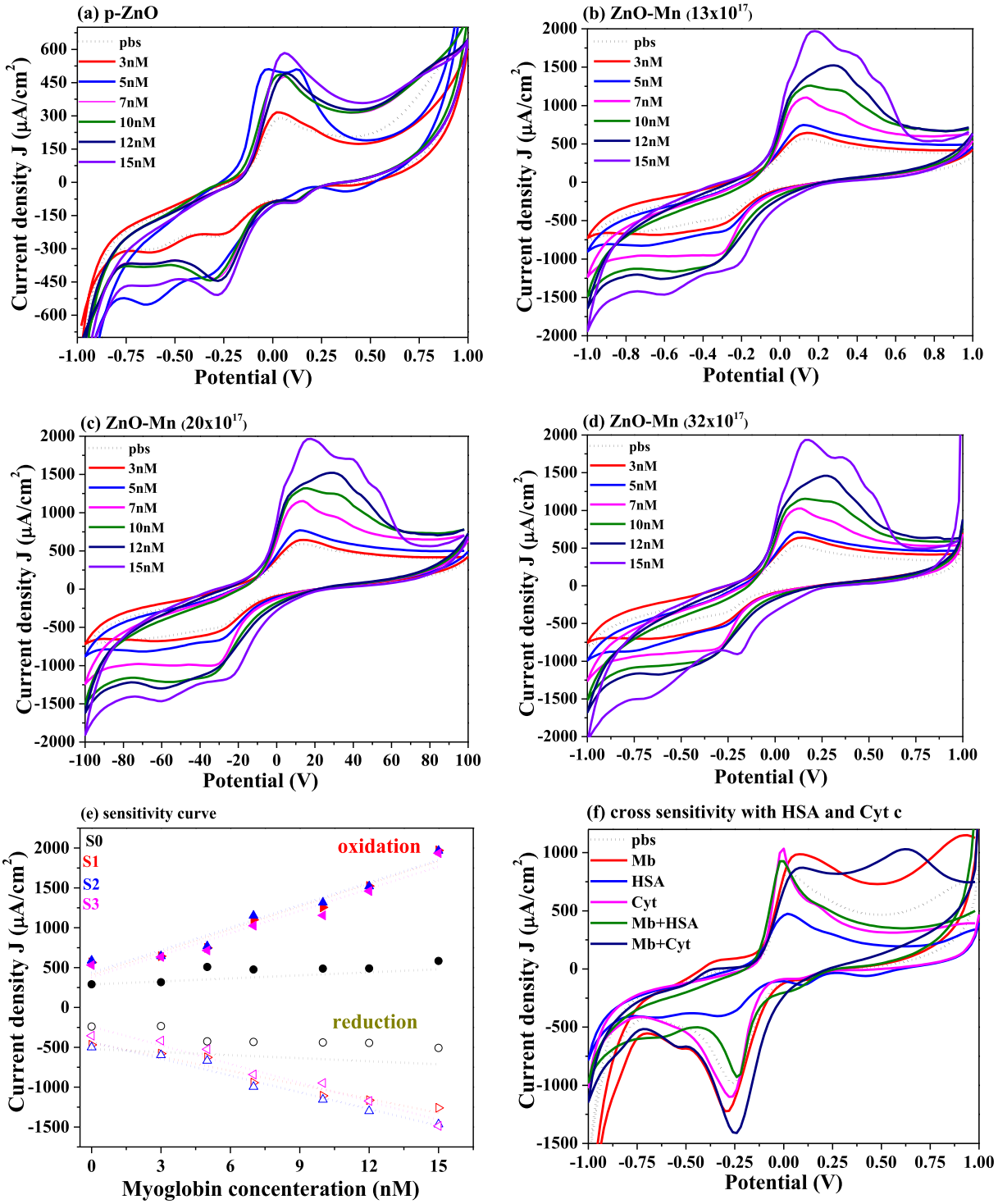

FIGURE 4. CV curves for different doping fractions (a) S0: pristine ZnO (b) S1: ZnO with Mn (13×10^{17}) (c) S2: ZnO with Mn (20×10^{17}) (d) S3: ZnO with Mn (32×10^{17}) (e) peak oxidation current plotted as a function of Mb concentration used as calibration curve to estimate unknown Mb concentration (symbol represents experimental data and dotted line is best fit), and (f) Interference study with Cytochrome c and HAS.

peaks are larger than pristine ZnO, is correlated to comparatively high density of states in doped samples. Peak separation increased from 180 mV for the buffer, up to 320 mV in the presence of Mb reflecting the reversible reaction for pristine and doped ZnO nanoparticles. The graph of peak current density (J) versus Mb concentration reveal linear and about four times increase of oxidation current intern sensitivity of Mb (Fig. 4(e)) for doped samples. Symbols demonstrate

experimental data while dotted line represent the best fit. The estimated sensitivity of 13 μA-cm^{-2}nM^{-1} is obtained for S0; pristine ZnO with LOD 2.88 nM. The sensitivity for doped samples is between 92-95 μA-cm^{-2}nM^{-1} whereas LOD is down between 0.35 nM to 0.42 nM (Table 1). The significant rise of sensitivity followed by Mn doping concentration is correlated to high density of states in doped samples originated from tensile strain. The marginal fall of sensitivity for S2 and S3 is correlated to reduction of tensile strain in the system at higher doping concentration. The limit of detection (LOD) is derived from the standard deviation using relation 3xS.D./slope; where slope is taken from the plot of peak current versus concentration graph. To the best of our knowledge, LOD of 0.35 nM is the lowest obtained against 0.45 nM in literature, we reported earlier [57] and are listed in Table 1. The high sensitivity of Mn doped ZnO compared to our earlier report of Cu doped ZnO is correlated to all half-filled 3d orbitals in Mn contributing three/four electrons for reaction unlike Cu which has completely filled 3d orbitals and can contribute only one/two electrons for reaction.

Fig. 4(f) depicts CV graphs obtained for the interference study with 5 mM human serum albumin (HSA), 7 nM Cytochrome c and 7 nM Mb obtained separately for estimation of the specificity of the investigated sensor. CV in phosphate buffer (PBS) was a reference and 1:1 volumetric mixture of Mb: HSA and Mb:cytochrome c solutions were tested. HSA concentration was chosen high as it is abundant in blood and cytorchrome c being a small hemeprotein is taken. The peak oxidation potential in buffer, Cytochrome c, Mb and HSA are recorded as 0.12 V, -0.004 V, -0.02 V and 0.02 V, respectively, while the peak potential value for the mixed solution of Mb-cytochrome c is 0.077 and that of Mb-HSA is -0.02 V. The sensor exhibit distinctive response to Mb, cytochrome c and HSA. The response time of the sensors was $\sim$10 ms.

To understand charge transfer features of developed sensors, CV plots were obtained for different scan rate from 10 to 100 mV/S at a fixed concentration of 7 nM of Mb (Fig. 5 a-d). High current density for both oxidation/reduction at fast scan rate found in all the samples lead by sinking of diffusion layer thickness. Additionally, noticeable shift of potential values towards lower energy with the increasing scan rate evident the same. Low value of $\Delta E_p = |E_a\text{-}E_c|$ indicates the fast electron transfer rate on the electrode surface. These results suggest a marginal change of reaction kinetics, though the reaction eventually attains the reversibility (Fig.5 (a)-(d)). Marginal increase in potential except S2 is correlated to the increase of effective thickness by deposit on the electrode surface during sensing impedes an electron transfer characteristics and partial diffusion control process. Besides shift of oxidation/reduction of peak oxidation potential, the potential difference between oxidation and reduction peak is independent of scan rate as evident from voltammograms (Fig.6(a)-(d)). This predicts a reversible electron transfer mechanism during the electrochemical reactions resulting free diffusion of redox species than deposition on surface of the electrode. The plot of peak current versus square root of scan rate exhibit linear variation of both oxidation and reduction current (Fig. 6(e)) suggest charge transfer at electrode surface is typically the diffusion controlled process. A graph of log of peak current as a function of the log of scan rate (Fig. 6(f)) fits linearly having slope of 0.57 which is close to theoretical value (0.5) for diffusion controlled process [58]. Slope of 0.7, 0.67 or more recommends the process is adsorption controlled and not a diffusion control. Also, it implies that some redox species might be either adsorbed or deposited on electrode surface owed to non-uniform distribution of ions and hence the rate limiting process.

Assuming reversible electron-transfer mechanism having free diffusion of redox ions, the diffusion coefficient for pure and doped ZnO is estimated from the Randles−Sevcik equation;

$$i_p = 0.4463.F.A.C.n^{3/2}(F\nu D/RT)^{1/2} \quad (2)$$

where i_p: maximum current (Amp), n: number of freely transferred electrons, A: electrode area in cm^2, F is Faraday's constant, C: concentration in Mole/cm^3, D: diffusion coefficient (cm^2/s), ν: scan rate (V/s), R:gas constant (JK^{-1}Mol^{-1}), and T: temperature in °K. The average value of diffusion coefficient is 5.5×10^{-5} cm^2/s, 6.1×10^{-6} cm^2/s, 3.2×10^{-6}cm^2/s and 3.0×10^{-6}cm^2/s for S0, S1, S2 and S3, respectively. The decrease of diffusion coefficient with doping concentration describes the time-rate of change of concentration in the system. This reveals that diffusion coefficient apparently increases i.e. the electron diffusion kinetics during the chemical reaction and electron transfer process varies with Mb doping concentration.

The influence of doping is further investigated using EIS study, separately acquired for all samples at different Mb concentrations. Fig. 6(a)-(e) represents four set of EIS data series as Nyquist plots for pure and doped ZnO (real and imaginary part of impedance). In general, for all samples, charge transfer resistance (R_{ct}) at the interface between electrolyte and sensing layer which was measured from radius of high frequency semicircle increases as a function of Mb concentration. This was interrelated to the increase of charge transfer density lead by the high density of Mb in the solution. The linear region at low frequency range corresponds to the diffusion within the active layer i.e. thickness of ZnO film. In general Fig. 6 (a)-(d), R_{ct} value was almost constant in PBS and upto 5 nM Mb concentration followed by consistent increase up to 15 nM exhibit almost linear characteristics (Fig. 6(a)-(e)). For doped samples, the value of R_{ct} increase linearly till 10 nM and then sharply rise manifesting non-linear behavior as a function of Mb concentration. R_{ct} values are high for doped samples in general and when compared individually for each Mb concentration (Fig. 6(b)-(e)). The minimum values of R_{ct} were obtained for S0 whereas maximum R_{ct} are recorded for S1 (Fig. 6(b); (e)). The sample S3 exhibit lowest charge transfer characteristics and hence less sensitivity in doped

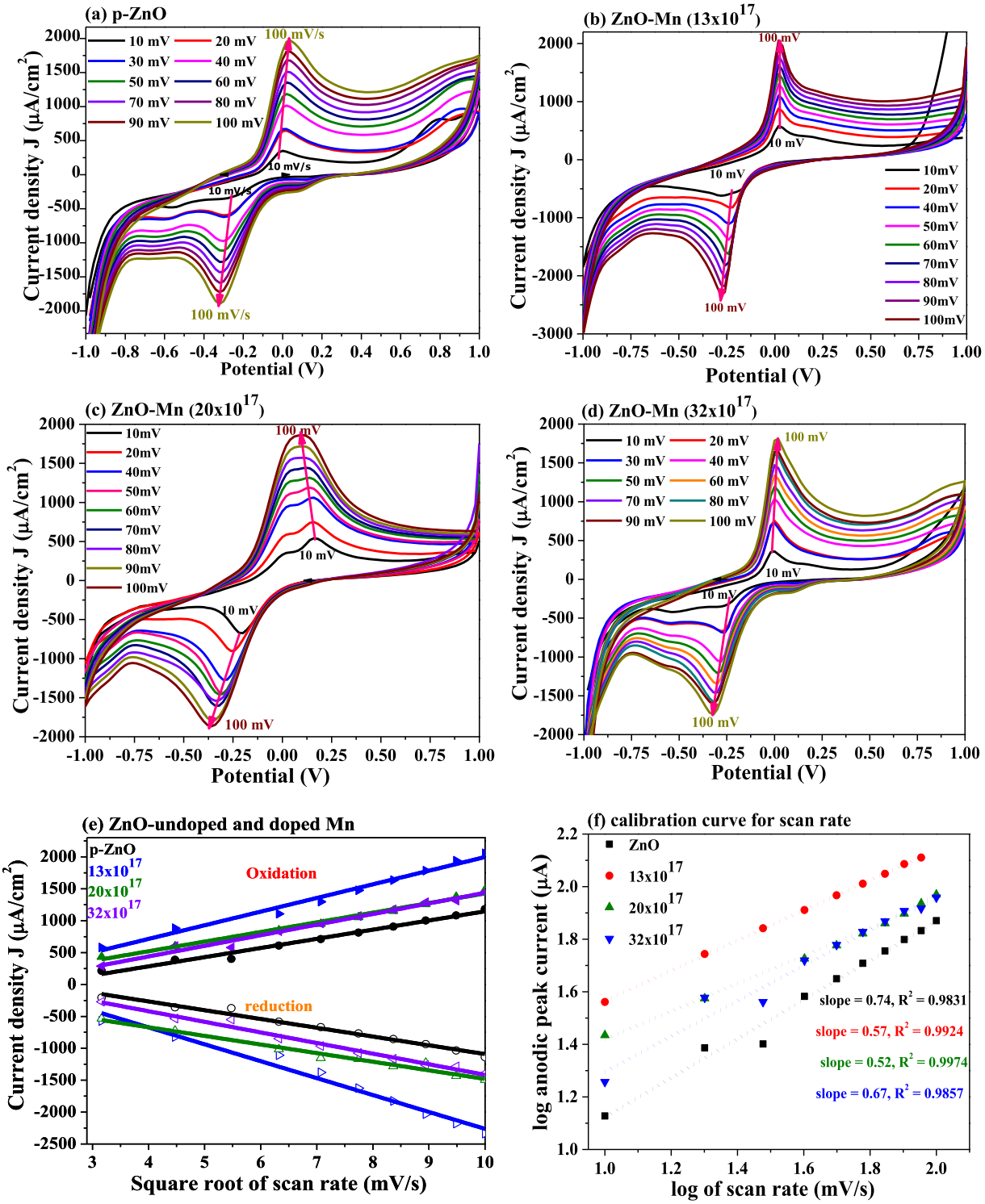

FIGURE 5. Effect of scan rate on the CV characteristics obtained at 5 nM of Mb for electrode made of (a) S0: pristine ZnO (b) S1; ZnO with 13 × 10^{17}Mn atoms/cm^3 (c) S2: ZnO with 20 × 10^{17}Mn atoms/cm^3 (d)S3: ZnO with 32 × 10^{17} Mn atoms/cm^3 (e) peak current (both oxidation and reduction) versus square root of scan rate, and (f) log of peak current (oxidation) versus log of scan rate show linear response. The symbol represents experimental data points and dotted line is the best fit obtained.

samples. Slow diffusion characteristics as implied from the large value of constant on the surface of pristine ZnO consequence to the sensing properties and low sensitivity.

Based on the sensing performance and various analyses, a possible mechanism of sensing is projected which demonstrates the electron transfer mechanism takes place during the

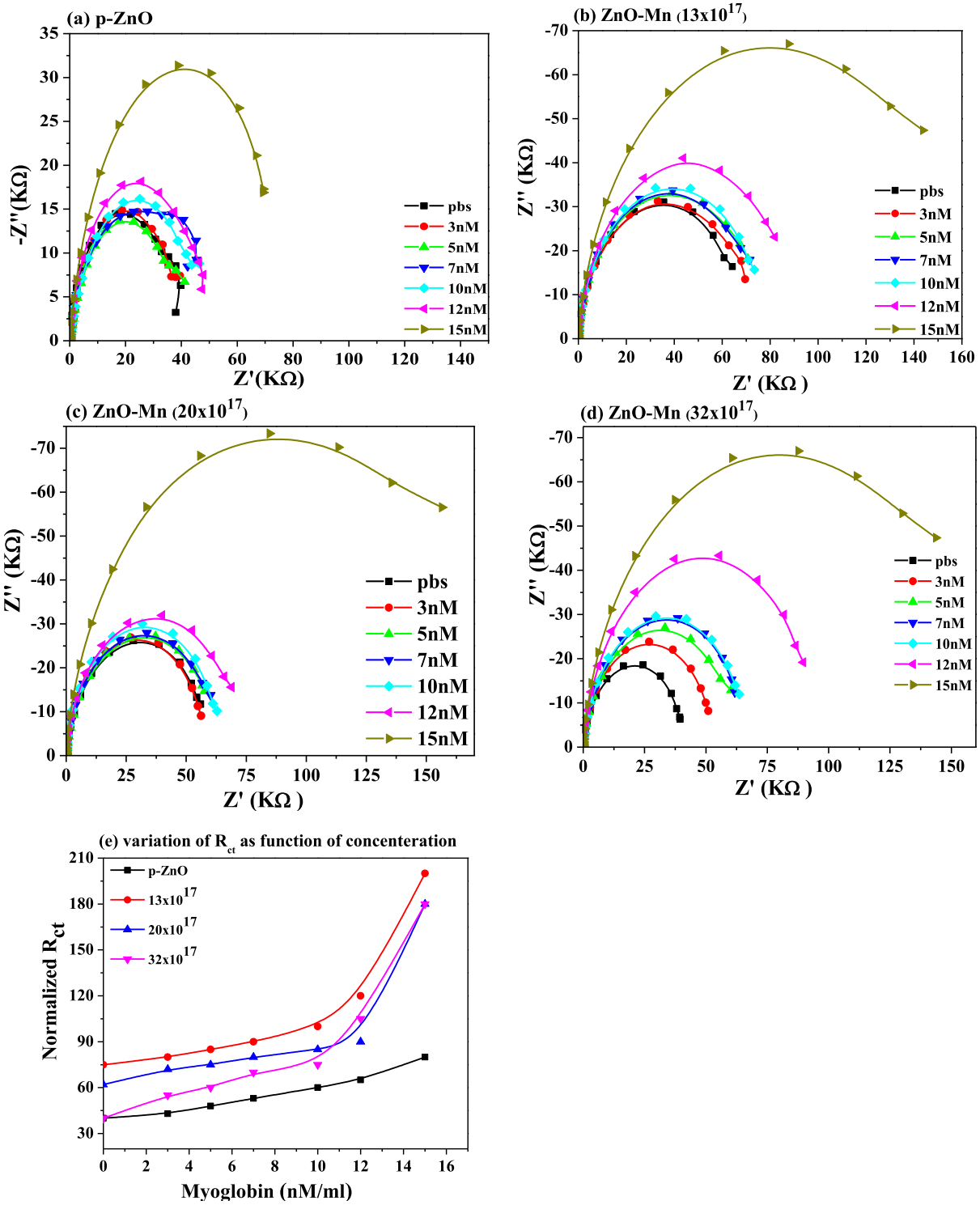

FIGURE 6. Series of Nyquist plots acquired for different Mb concentration for as synthesized ZnO nanopowders (a) pristine ZnO (b) ZnO-Mn(13×10^{17}) (c) ZnO-Mn (20×10^{17}) (d) ZnO-Mn (32×10^{17}) and (e) R_{ct} values of Mb at 3–15 nM in pbs.

redox reaction as shown in Fig. 7(a)-(b). Fig. 7(a) reveals the steps and reaction mechanism involved during sensing whereas Fig.7(b) depicts charge transfer characteristics. Basically, Mb exists in an oxidized form owing to presence of Fe ion, which is a known redox couple. While sensing, the moment applied potential at the electrode rises above $E^{1/2}$ the electron from material is transferred to Mb converting from Fe^{3+} to Fe^{2+} reducing Mb and oxidizing ZnO film on working electrode exhibits the increase of oxidative current. Increase in the degree of oxidation of ZnO is evidence from absorption study shown in Fig.3. In contrary, during the negative sweep when applied potential reaches

(a) Proposed sensing mechanism

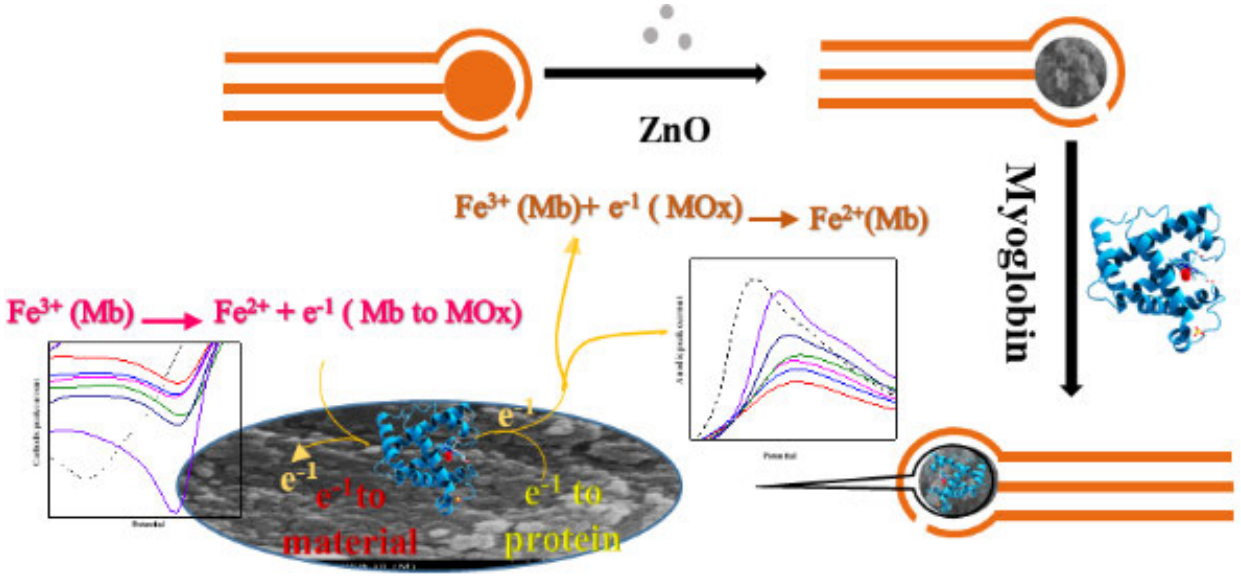

(b)

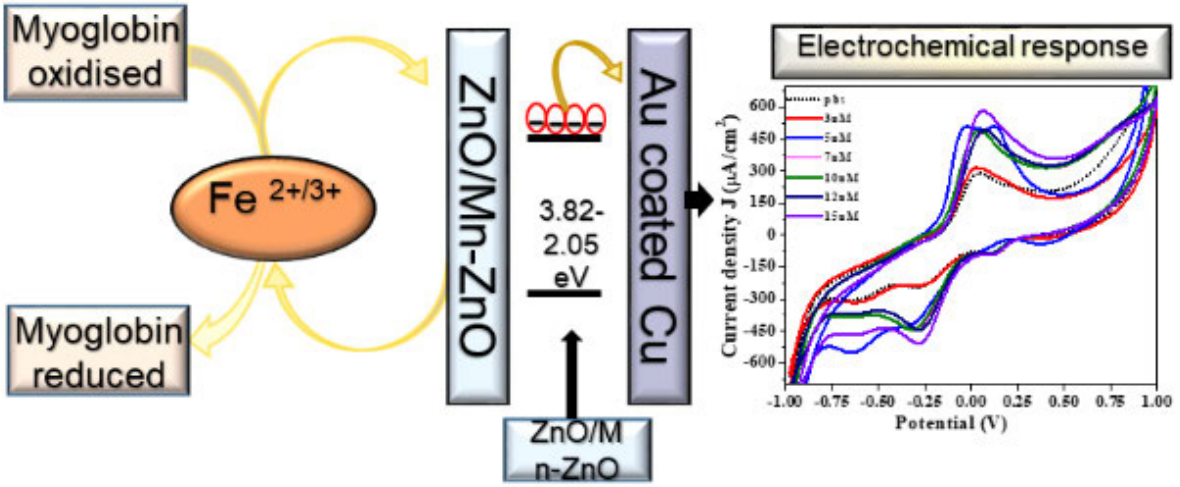

FIGURE 7. Proposed sensing mechanism.

to equilibrium, electron transfer takes place from Mb to the electrode (ZnO film) wherein Fe^{2+} is converted to Fe^{3+} state releasing an electron to ZnO film (electrode) and reduction current is monitored. Fig. 7(b) is summarizing the electron transfer phenomena which involve a single and reversible electron transfer in the process which enables the sensing at higher Mb concentrations. The shift of peak potentials and different current values observed from the scan rate study are associated to several interfering factors arising from surface and physical status of electrodes with time.

IV. CONCLUSION

Pristine and Mn doped ZnO nanoparticles, with different Mn concentrations (13×10^{17}, 20×10^{17} and 32×10^{17} atoms/cm^3) in ZnO matrix, prepared using sol-gel method exhibit distinct structural and optical properties. X-ray diffraction revealed mixed phases of $Zn_2Mn_3O_8$ along with pure ZnO phases. A band around 665 cm^{-1} in FTIR spectra confirms synthesis of metal oxide nanoparticles. Average particle size of ∼70-90 nm obtained from XRD is in agreement with FESEM results. An optical band gap was decreased sharply from 3.82 eV for pristine ZnO to 2.05eV lowest for Mn doped ZnO with 13×10^{17} atoms/cm^3 (S1) whereas spherical nanoparticles are systematically transformed to nanobelt like structures with Mn doping in ZnO matrix from S0-S3. An electrochemical device fabricated for Mb using pristine and Mn doped ZnO show different sensitivity towards myoglobin (Mb). CV and scan rate curves indicate a reversible reaction suggesting the possible reusability. The sensitivity plots acquired from oxidation and reduction current as a

TABLE 2. Reported LOD values based on method of detection and matrix.

Method	Method/sample matrix	Amplification signal	Sensitivity	LOD value	Ref.
Electrochemical	nickel oxide and graphene modified carbon electrode carbon	current/resistance	35μA/mM	0.23 mM	[32]
Immunosensor	gold nanoparticle based Immunosensor	current/resistance	10 μA /(ng/ml)	5.5 ng/ml	[33]
Electrochemical (EIS)	Ag-Mb	current/resistance	0.1mA/(ng/ml)	2.7 ng/ml	[34]
Electrochemical immunosensor	CuS–MoS_2	current	21.06 μA/(ng/ml)	1.2 pg/ml (~68 nM)	[35]
Electrochemical	Ti-NT/GCE	current	18 μA(mg/ml)	1 μg/ml	[36]
Electrochemical	rGO/CNT/SPE	current	1.01 μA- cm^2 (ng/ml)	0.34 ng/ml	[37]
Electrochemical	Fe_3O_4@SiO_2 microsphere	current	31.57μA/(mM/L)	0.48μM	[38]
Electrochemical	SPE-Mn doped ZnO nanoparticles, buffer	current/resistance	**S0: 13 μA-cm^{-2} / nM** **S1: 95μA-cm^{-2} / nM** **S2: 94μA-cm^{-2}/ nM** **S3: 92μA-cm^{-2} / nM**	2.88 nM 0.35 nM 0.39 nM 0.42 nM	current work

*** S0;ZnO, S1;ZnO-Mn (Mn=13x 10^{17}), S2; ZnO-Mn (Mn=20x10^{17}), S3; ZnO-Mn (Mn=32x10^{17})**

function of concentration reflects that doping induces 7 times increases in sensitivity than that of pristine ZnO. Electrochemical sensor fabricated using 13 × 10^{17} atoms/cm^3 Mn doped ZnO exhibit highest sensitivity of 95 $\mu Acm^{-2}nM^{-1}$ with LOD of 0.35 nM which is lowest reported so far, to the best of our knowledge (Table 2). The sensor has high sensitivity with response time of ∼10 ms even at low Mb concentrations and linear response over wider range of Mb. The interference study against Cytochrome c and HSA exhibit different peak oxidation and reduction potential and current values suggest the selective response towards Mb. The developed material and sensor demonstrate promising and reliable results with device potential and can be an excellent sensing platform for rapid detection of AMI.

ACKNOWLEDGMENT

The authors would like to acknowledge the Central Instrumentation Facility and DST-PURSE program of Jamia Millia Islamia, New Delhi.

CONFLICTS OF INTEREST

There are no conflicts to declare by authors

REFERENCES

[1] Q. Gao, Y. Dai, B. Han, W. Zhu, X. Li, and C. Li, "Enhanced gas-sensitivity and ferromagnetism performances by the ni-doping induced oxygen vacancies in (mn, Ni) codoped ZnO nanorods," *Appl. Surf. Sci.*, vol. 490, pp. 178–187, Oct. 2019.

[2] J. Anghel, "Correlation between saturation magnetization, bandgap, and lattice, volome of, transition metal (M= Cr, Mn, Fe, Co, or Ni) doped Zn_1 xM xO nanoparticles," *J. Appl. Phys.*, vol. 107, May 2010, Art. no. 09E314.

[3] S. C. Das, R. J. Green, J. Podder, T. Z. Regier, G. S. Chang, and A. Moewes, "Band gap tuning in ZnO through ni doping via spray pyrolysis," *J. Phys. Chem. C*, vol. 117, no. 24, pp. 12745–12753, Jun. 2013.

[4] D. A. A. Santos and M. A. Macádo, "Study of the magnetic and structural properties of Mn-, Fe-, and co-doped ZnO powder," *Phys. B, Condens. Matter*, vol. 407, no. 16, pp. 3229–3232, Aug. 2012.

[5] M. Shatnawi, A. M. Alsmadi, I. Bsoul, B. Salameh, M. Mathai, G. Alnawashi, G. M. Alzoubi, F. Al-Dweri, and M. S. Bawa'aneh, "Influence of mn doping on the magnetic and optical properties of ZnO nanocrystalline particles," *Results Phys.*, vol. 6, pp. 1064–1071, 2016.

[6] A. A. Othman, M. A. Osman, E. M. M. Ibrahim, M. A. Ali, and A. G. Abd-Elrahim, "Mn-doped ZnO nanocrystals synthesized by sonochemical method: Structural, photoluminescence, and magnetic properties," *Mater. Sci. Eng., B*, vol. 219, pp. 1–9, May 2017.

[7] W. H. W. Tang, G. S. Francis, D. A. Morrow, L. K. Newby, C. P. Cannon, R. L. Jesse, A. B. Storrow, R. H. Christenson, R. H. Christenson, F. S. Apple, C. P. Cannon, G. S. Francis, R. L. Jesse, D. A. Morrow, L. K. Newby, A. B. Storrow, W. H. W. Tang, and A. H. B. Wu, "National academy of clinical biochemistry laboratory medicine practice guidelines: Clinical utilization of cardiac biomarker testing in heart failure," *Clin. Biochem.*, vol. 41, nos. 4–5, pp. 210–221, Mar. 2008.

[8] V. L. Roger, "Heart disease and stroke statistics-2011 update: A report from the American Heart Association," *Circulatation*, vol. 123, pp. 209–218, May 2011.

[9] A. L. Straface, J. H. Myers, H. J. Kirchick, and K. E. Blick, "A rapid point-of-care cardiac marker testing strategy facilitates the rapid diagnosis and management of chest pain patients in the emergency department," *Amer. J. Clin. Pathol.*, vol. 129, no. 5, pp. 788–795, May 2008.

[10] J. Zhu, N. Zou, H. Mao, P. Wang, D. Zhu, H. Ji, H. Cong, C. Sun, H. Wang, F. Zhang, J. Qian, Q. Jin, and J. Zhao, "Evaluation of a modified lateral flow immunoassay for detection of high-sensitivity cardiac troponin i andmyoglobin," *Biosensors Bioelectron.*, vol. 42, pp. 522–525, Apr. 2013.

[11] *Cardiovascular Diseases*, WHO, Geneva, Switzerland, 2017.

[12] E. J. Benjamin, "Heart disease and stroke statistics-2017 update: A report from the American Heart Association," *Circulatation*, vol. 135, pp. 146–603, Oct. 2017.

[13] E. Wilkins, L. Wilson, K. Wickramasinghe, P. Bhatnagar, J. Leal, R. Luengo-Fernandez, R. Burns, M. Rayner, and N. Townsend, "European cardiovascular disease statistics 2017," Eur. Heart Netw., Brussels, Belgium, Tech. Rep., 2017.

[14] D. Prabhakaran, "Cardiovascular diseases in India compared with the United States," *J. Amer. College Cardiol.*, vol. 72, pp. 79–95, May 2018.

[15] A. S. Jaffe, "Biomarkers in acute cardiac disease: The present and the future," *J. Amer. College Cardiol.*, vol. 48, pp. 1–11, Dec. 2006.

[16] J. McCord, "Ninety-minute exclusion of acute myocardial infarction by use of quantitative point-of-care testing of myoglobin and troponin I," *Circulatation*, vol. 104, pp. 1483–1488, 2001.

[17] S. M. Sallach, R. Nowak, M. P. Hudson, G. Tokarski, N. Khoury, M. C. Tomlanovich, G. Jacobsen, J. A. de Lemos, and J. McCord, "A change in serum myoglobin to detect acute myocardial infarction in patients with normal troponin i levels," *Amer. J. Cardiol.*, vol. 94, no. 7, pp. 864–867, Oct. 2004.

[18] G. Giannopoulos, S. Deftereos, V. Panagopoulou, C. Kossyvakis, A. Kaoukis, G. Bouras, V. Pyrgakis, and M. W. Cleman, "Copeptin as a biomarker in cardiac disease," *Current Topics Med. Chem.*, vol. 13, no. 2, pp. 231–240, Mar. 2013.

[19] S. J. Aldous, "Cardiac biomarkers in acute myocardial infarction," *Int. J. Cardiol.*, vol. 164, no. 3, pp. 282–294, Apr. 2013.

[20] S. Pervaiz, "Comparative analysis of cardiac troponin I and creatine kinase MB as markers of acute myocardial infarction," *Clin. Cardiol.*, vol. 20, pp. 269–271, 1997.

[21] J. Kendrew, "The species specificity of myoglobin," *Nature*, vol. 174, p. 946, 1954.

[22] A. Qureshi, Y. Gurbuz, and J. H. Niazi, "Biosensors for cardiac biomarkers detection: A review," *Sens. Actuators B, Chem.*, vols. 171–172, pp. 62–76, Aug. 2012.

[23] B. McDonnell, S. Hearty, P. Leonard, and R. O'Kennedy, "Cardiac biomarkers and the case for point-of-care testing," *Clin. Biochem.*, vol. 42, nos. 7–8, pp. 549–561, May 2009.

[24] Z. Yang and D. Min Zhou, "Cardiac markers and their point-of-care testing for diagnosis of acute myocardial infarction," *Clin. Biochem.*, vol. 39, no. 8, pp. 771–780, Aug. 2006.

[25] J.-F. Masson, T. M. Battaglia, P. Khairallah, S. Beaudoin, and K. S. Booksh, "Quantitative measurement of cardiac markers in undiluted serum," *Anal. Chem.*, vol. 79, no. 2, pp. 612–619, Jan. 2007.

[26] I.-H. Cho, E.-H. Paek, Y.-K. Kim, J.-H. Kim, and S.-H. Paek, "Chemiluminometric enzyme-linked immunosorbent assays (ELISA)-on-a-chip biosensor based on cross-flow chromatography," *Anal. Chim. Acta*, vol. 632, no. 2, pp. 247–255, Jan. 2009.

[27] V. V. Shumyantseva, T. V. Bulko, M. Y. Vagin, E. V. Suprun, and A. I. Archakov, "Electrochemical immunoanalysis of cardiac myoglobin," *Biochemistry*, vol. 4, no. 3, pp. 237–242, Sep. 2010.

[28] B. A. Wittenberg and J. B. Wittenberg, "Transport of oxygen in muscle," *Annu. Rev. Physiol.*, vol. 51, pp. 857–878, May 1989.

[29] L. Dobáa and K. Cullen Edozien, "Copeptin and its potential role in diagnosis and prognosis of various diseases," *Biochemia, Biochemia medica*, vol. 23, pp. 172–190, 2013.

[30] J. S. Alpert, "Myocardial infarction redefined—A consensus document of The Joint European society of cardiology/American college of cardiology committee for the redefinition of myocardial infarction," *J. Amer. College Cardiol.*, vol. 36, pp. 959–969, May 2000.

[31] M. Wolf, D. Juncker, B. Michel, P. Hunziker, and E. Delamarche, "Simultaneous detection of C-reactive protein and other cardiac markers in human plasma using micromosaic immunoassays and self-regulating microfluidic networks," *Biosensors Bioelectron.*, vol. 19, no. 10, pp. 1193–1202, May 2004.

[32] O. V. Gnedenko, Y. V. Mezentsev, A. A. Molnar, A. V. Lisitsa, A. S. Ivanov, and A. I. Archakov, "Highly sensitive detection of human cardiac myoglobin using a reverse sandwich immunoassay with a gold nanoparticle-enhanced surface plasmon resonance biosensor," *Analytica Chim. Acta*, vol. 759, pp. 105–109, Jan. 2013.

[33] B. Osman, L. Uzun, N. Beáirli, and A. Denizli, "Microcontact imprinted surface plasmon resonance sensor for myoglobin detection," *Mater. Sci. Eng., C*, vol. 33, no. 7, pp. 3609–3614, Oct. 2013.

[34] L. Tang and K. A. Kang, "Preliminary study of fiber optic multi-cardiac-marker biosensing system for rapid coronary heart disease diagnosis and prognosis," in *Oxygen Transpotation to Tissue*. Cham, Switzerland: Springer, 2006, pp. 101–106.

[35] W.-Y. Wu, "PDMS gold nanoparticle composite film-based silver enhanced colorimetric detection of cardiac troponin I," *Sens. Actuators B, Chem.*, vol. 147, pp. 298–303, 2010.

[36] E. V. Suprun, A. L. Shilovskaya, A. V. Lisitsa, T. V. Bulko, V. V. Shumyantseva, and A. I. Archakov, "Electrochemical immunosensor based on metal nanoparticles for cardiac myoglobin detection in human blood plasma," *Electroanalysis*, vol. 23, no. 5, pp. 1051–1057, May 2011.

[37] I. Lee, X. Luo, X. T. Cui, and M. Yun, "Highly sensitive single polyaniline nanowire biosensor for the detection of immunoglobulin g and myoglobin," *Biosensors Bioelectron.*, vol. 26, no. 7, pp. 3297–3302, Mar. 2011.

[38] G. Mandal, "Mode of bindings of zinc oxide nanoparticles to myoglobin and horseradish peroxidase: A spectroscopic investigations," *J. Appl. Phys.*, vol. 110, Apr. 2011, Art. no. 024701.

[39] S. K. Mishra, D. Kumar, A. M. Biradar, and Rajesh, "Electrochemical impedance spectroscopy characterization of mercaptopropionic acid capped ZnS nanocrystal based bioelectrode for the detection of the cardiac biomarker—Myoglobin," *Bioelectrochemistry*, vol. 88, pp. 118–126, Dec. 2012.

[40] F. T. C. Moreira, R. A. F. Dutra, J. P. C. Noronha, and M. G. F. Sales, "Electrochemical biosensor based on biomimetic material for myoglobin detection," *Electrochimica Acta*, vol. 107, pp. 481–487, Sep. 2013.

[41] F. T. C. Moreira, S. Sharma, R. A. F. Dutra, J. P. C. Noronha, A. E. G. Cass, and M. G. F. Sales, "Smart plastic antibody material (SPAM) tailored on disposable screen printed electrodes for protein recognition: Application to myoglobin detection," *Biosensors Bioelectron.*, vol. 45, pp. 237–244, Jul. 2013.

[42] M. J. Whitcombe, I. Chianella, L. Larcombe, S. A. Piletsky, J. Noble, R. Porter, and A. Horgan, "The rational development of molecularly imprinted polymer-based sensors for protein detection," *Chem. Soc. Rev.*, vol. 40, no. 3, pp. 1547–1571, 2011.

[43] D. Chen, L. Tang, and J. Li, "Graphene-based materials in electrochemistry," *Chem. Soc. Rev.*, vol. 39, no. 8, pp. 3157–3180, 2010.

[44] W. Sun, S. Gong, Y. Deng, T. Li, Y. Cheng, W. Wang, and L. Wang, "Electrodeposited nickel oxide and graphene modified carbon ionic liquid electrode for electrochemical myglobin biosensor," *Thin Solid Films*, vol. 562, pp. 653–658, Jul. 2014.

[45] X. Ren, "Development of electrochemical impedance immunosensor for sensitive determination of myoglobin," *Int. J. Electrochem. Sci.*, vol. 15, pp. 7765–7776, Aug. 2017.

[46] L. Sun, "Development of an electrochemical impedance immunosensor for myoglobin determination," *Int. J. Electrochem. Sci.*, vol. 7, pp. 6170–6179, Jul. 2017.

[47] B. Zhang, Y. Zhang, W. Liang, X. Yu, H. Tan, G. Wang, A. Li, J. Jin, and L. Huang, "Copper sulfide-functionalized molybdenum disulfide nanohybrids as nanoenzyme mimics for electrochemical immunoassay of myoglobin in cardiovascular disease," *RSC Adv.*, vol. 7, no. 5, pp. 2486–2493, 2017.

[48] S. S. Mandal, "Employing denaturation for rapid electrochemical detection of myoglobin using TiO_2 nanotubes," *J. Mater. Chem. B*, vol. 1, pp. 3051–3056, Aug. 2013.

[49] V. Kumar, "Graphene-CNT nanohybrid aptasensor for label free detection of cardiac biomarker myoglobin," *Biosensors Bioelectron.*, vol. 72, pp. 56–60, Jun. 2015.

[50] X. Wang, Z. You, H. Sha, Z. Sun, and W. Sun, "Electrochemical myoglobin biosensor based on carbon ionic liquid electrode modified with Fe SiO_2 microsphere," *J. Solid State Electrochemistry*, vol. 18, no. 1, pp. 207–213, Jan. 2014.

[51] F. Achouri, S. Corbel, L. Balan, K. Mozet, E. Girot, G. Medjahdi, M. B. Said, A. Ghrabi, and R. Schneider, "Porous mn-doped ZnO nanoparticles for enhanced solar and visible light photocatalysis," *Mater. Des.*, vol. 101, pp. 309–316, Jul. 2016.

[52] B. Cullity, *Elements of X-Ray Diffraction*, 3rd ed. Upper Saddle River, NJ, USA: Prentice-Hall, 2001.
[53] S. G. Ansari, P. Boroojerdian, S. R. Sainkar, R. N. Karekar, R. C. Aiyer, and S. K. Kulkarni, "Grain size effects on H_2 gas sensitivity of thick film resistor using SnO_2 nanoparticles," *Thin Solid Films*, vol. 295, nos. 1–2, pp. 271–276, Feb. 1997.
[54] M. Haque, H. Fouad, H.-K. Seo, O. Y. Alothman, and Z. A. Ansari, "Cu-doped ZnO nanoparticles as an electrochemical sensing electrode for cardiac biomarker myoglobin detection," *IEEE Sensors J.*, vol. 20, no. 15, pp. 8820–8832, Aug. 2020.
[55] S. G. Ansari, R. Wahab, Z. A. Ansari, Y.-S. Kim, G. Khang, A. Al-Hajry, and H.-S. Shin, "Effect of nanostructure on the urea sensing properties of sol–gel synthesized ZnO," *Sens. Actuators B, Chem.*, vol. 137, no. 2, pp. 566–573, Apr. 2009.
[56] Y.-W. Lee and K.-B. Song, "Effect of α-Irradiation on the molecular properties of myoglobin," *BMB Rep.*, vol. 35, no. 6, pp. 590–594, Nov. 2002.
[57] Q. Wang, X. Yang, X. Yang, F. Liu, and K. Wang, "Visual detection of myoglobin via G-quadruplex DNAzyme functionalized gold nanoparticles-based colorimetric biosensor," *Sens. Actuators B, Chem.*, vol. 212, pp. 440–445, Jun. 2015.
[58] D. Thomas, Z. Rasheed, J. S. Jagan, and K. G. Kumar, "Study of kinetic parameters and development of a voltammetric sensor for the determination of butylated hydroxyanisole (BHA) in oil samples," *J. Food Sci. Technol.*, vol. 52, no. 10, pp. 6719–6726, Oct. 2015.

MAZHARUL HAQUE received the integrated M.Sc. degree in bioinformatics and biotechnology and the M.Phil. degree in basic sciences from the Centre for Interdisciplinary Research in Basic Sciences, Jamia Millia Islamia, New Delhi, India, in 2016. He is currently pursuing the Ph.D. degree in nanobiotechnology. His research interests include synthesis and characterization of nanoparticles and their application in biosensing especially biomarkers responsible in acute myocardial infarction (AMI) commonly known as heart attack.

HASSAN FOUAD studied at Helwan University, Egypt, for the B.Sc. and M.Sc., in 1990 and 1996, respectively. He obtained his Ph.D. degree in the field of biomedical polymers from Helwan and Leeds University, in 2000. He has worked as a Research Scientist with the Vienna University of Technology. He is currently a Full Professor of biomaterials and tissue engineering with King Saud University and Helwan University.

HYUNG-KEE SEO received the Ph.D. degree in chemical engineering from Jeonbuk National University, South Korea, in 2006. From 2008 to 2012, he has worked as a Postdoctoral Researcher with the Department of Chemistry, Colorado State University, USA. He is currently an Associate Professor with the School of Chemical Engineering, Jeonbuk National University. His current research interests include sensors, solar cells, and photocatalyst application.

ALOTHMAN Y. OTHMAN received the B.Sc. degree in chemical engineering from King Saud University, in 1997, and the Ph.D. degree in polymer science and technology from The University of Manchester, in 2007. He is currently a Professor with the Department of Chemical Engineering, King Saud University, with more than 12 years in teaching of undergraduate and graduate levels. He has published and presented more than 100 papers in journals and conferences, in addition to coediting and translating five books. His research interests include polymer processing, blends, and additives, including processing, aging, and characterization of natural fiber/polymer composites, with an interest on the environmental aspects.

ATUL KULKARNI received the M.S. degree from the Department of Instrumentation Science, University of Pune, India, in 1995, and the Ph.D. degree from the Department of Physics, University of Pune, in 2005. He was with the Department of Mechanical Engineering, Sungkyunkwan University (SKKU), South Korea, under the Brain Korea Plus (BK21+) Fellowship. He is currently associated with the Symbiosis Centre for Nanoscience and Nanotechnology (SCNN), Symbiosis International (Deemed University), India, as a Research Professor and the Director. During and prior to his Ph.D. pursuit, he has worked in Indian industries for more than 17 years (from 1989 to 2005) in different disciplines. In December 2006, he was offered Postdoctoral Fellowship at SKKU. Since then, he is actively involved in nanoscience and nanotechnology for materials synthesis and multidisciplinary sensor development. In the recent past, he has published more than 100 research articles in peer-reviewed international journals. There are 15 patents (Indian, Korean, U.S., and PCT) to his credit.

Z. A. ANSARI received the Ph.D. degree in applied physics from the University of Pune, India, in 1998. She was a Lecturer with the Department of Physics and the Department of Electronic Science, University of Pune. She has worked as a Research Professor with Inha University and Chonbuk National University, South Korea. She was a JSPS Fellow and then an Assistant Professor with the School of Material Science, Japan, and the Advanced Institute of Science and Technology, Ishikawa. She is currently a Professor of physics with the Centre for Interdisciplinary Research in Basic Sciences, Jamia Millia Islamia, New Delhi, India. Her current research interests include nanoscience and technology, and surface science and microscopy.